Supplementary Information

One-step dual-additive passivated wide-bandgap perovskites to realize 44.72%-efficient indoor photovoltaics

Qiaoyan Ma[1,†], Yousheng Wang[1,2,†,*], Liming Liu[1], Peng Yang[1], Wujie He[1], Xing Zhang[1], Jianzha Zheng[1], Mengen Ma[1], Meixiu Wan[1,2], Yuzhao Yang[1], Cuiling Zhang[3], Tahmineh Mahmoudi[4], Shaohang Wu[1,2,3], Chong Liu[1,2,3], Yoon-Bong Hahn[4], Yaohua Mai[1,2,3,*]

[1]Institute of New Energy Technology, College of Physics & Optoelectronic Engineering, Jinan University, Guangzhou 510632, China

[2]Key Laboratory of New Semiconductors and Devices of Guangdong Higher Education Institutes, Jinan University, Guangzhou 510632, China

[3]Guangdong Mellow Energy Co., Ltd., Guangzhou 510630, China

[4]School of Semiconductor and Chemical Engineering, Solar Energy Research Center, Jeonbuk National University, 567 Baekjedaero, Deokjin-gu, Jeonju-si, Jeollabuk-do, 54896 Republic of Korea

*Corresponding author: wangys0120@jnu.edu.cn and yaohuamai@jnu.edu.cn

†These authors contributed equally to this work.

Experimental Part

Materials

Formamidinium iodide (≥99.5%) was purchased from Greatcell Solar, Australia. Methylammonium bromide (≥99.995%), lead iodide (≥99.99%), lead bromide (99.99%) and cesium iodide (99.999%) were purchased from Xi'an e-Light New Matenal Company limited. Phenethylammonium (>99.5%), C60, Oleylammonium lodide (OAmI) and Poly[bis(4-phenyl) (2,4,6-trimethylphenyl) amine were purchased from Xi'an polymer Light Technology Corp. N, N-dimethylformamide (99.8%), dimethyl sulfoxide (>99.9%), isopropanol (≥99.9%), ethyl acetate (≥99%) and Trichloromethane ($CHCl_3$, ≥99%) were purchased from Aladdin. The Al_2O_3 dispersion (30 nm, 20 wt% in isopropanol) was purchased from Sigma-Aldrich. Toluene (≥99.9%) was purchased from Guangzhou Chemical Reagent Factory. All the reagents were used as received without further purification.

Preparation of perovskite precursor

The perovskite precursor solution was prepared by mixing CsI, $FAPbI_3$ and $MAPbBr_3$ solution in mixed solvent (DMF:DMSO=4:1) with a chemical formula of $Cs_{0.05}FA_{0.70}MA_{0.25}PbI_{2.25}Br_{0.75}$ (E_g=1.71 eV). Firstly, a CsI solution (1.5 M) was prepared by dissolving CsI in DMSO solvent; Both (1.5 M, with 8% excess of PbI_2) and $MAPbBr_3$ (1.5 M) solutions were prepared by dissolving FAI and PbI_2, and MABr and $PbBr_2$ into the mixed solvents (volume ratio of DMF:DMSO=4:1), respectively; Then, the desired perovskite precursor solution was formed by mixing pre-prepared $FAPbI_3$, $MAPbBr_3$, CsI, and DMSO solutions with a volume ratio of 15:5:1:1; Finally, the as-prepared perovskite precursor solution was further heated on a hotplate at 55 ℃, and then the pre-prepared Oleylammonium lodide (OAmI) solution in trichloromethane ($CHCl_3$) with different contents was added into perovskite precursor.

Theoretical simulation

The density functional theory calculations were performed using a Dmol3 module of Material Studio 2020. The generalized gradient approximation (GGA) method with Perdew-Burke-Ernzerhof (PBE) function was employed to describe the interactions between core and electrons. The force and energy convergence criterion were set to 0.002 Ha Å^{-1} and 10^{-5} Ha, respectively. When the optimization was completed, the ESP calculations were performed.[1,2]

Devices fabrication

Preparation of NiO_x/polymer PTAA was similar our previous works:[3,4] ITO glass substrates were sequentially washed with detergent, deionized water and isopropanol by ultrasonication for 20 min, and then dried with N_2. The NiO_x layer (20 nm) was deposited on ITO glass substrates at room temperature by sputtering NiO target (99.9%) using RF magnetron sputter system (SHENYANG QIHUI VACUUM TECHNOLOGY CO., LTD). A radio frequency (RF) power of 65 W, base pressure of the chamber of 7.9×10^{-4} Pa, working pressure of 2 Pa and Argon gas flux of 20 sccm were used to obtain high-quality NiO_x films. PTAA layer was deposited on the NiO_x film by using spin-coating PTAA solution in toluene (TL) solvent (1.5 mg mL^{-1}) at 6000 rpm for 30 s, followed by annealing at 120 °C for 20 min. Al_2O_3 solution (1 mL 20 wt% colloidal Al_2O_3 was diluted in 50 mL IPA) was spin coated successively on the ITO/NiO_x/PTAA substrate at 3500 rpm for 30 s, respectively (As reported in our previous works,[3,5] the presence of mp-Al_2O_3 not only can improve the contact interface at PTAA/perovskite but also facilitate charge extraction and transport by effective electron blocking).

The ITO/NiO_x/PTAA/mp-Al_2O_3 substrates were transferred to glovebox. The perovskite layer was deposited on the above substrates by spin-coating perovskite solutions using a consecutive two-steps program consisting of 1000 rpm for 4 s and 4000 rpm for 30 s. During the second step, the ethyl acetate (EA) was dropped onto the substrate at 10 s before the end of the program. The films were then annealed at 100 °C for 20 min. Next, PEAI solution in isopropanol (IPA) solvent (1 mg mL^{-1}) was deposited on the top of perovskite films by using spin-coating method at 3400 rpm for 30 s, followed by annealing at 100 °C for 10 min. Then C_{60} layer (30 nm) was prepared by evaporating method using a thermal evaporator (QHV-R53). Next the ALD-SnO_2 layer was prepared by using an atomic layer deposition (ALD) System (Dongguan Nanofrontier Microelectronics). The TDMASn and H_2O were used as precursors for the ALD deposition at 100 °C and with 200 cycles to obtain the ALD-SnO_2 buffer layer (~30 nm). Finally, the top electrode silver (150 nm) was deposited by a thermal evaporator (QHV-R53).

Characterization and Measurements

The surface morphology of perovskite films and cross-sectional view of device configuration were examined by scanning electron microscopy (SEM, FEI Apreo LoVac). The surface morphology status further was measured by tapping-mode atomic force microscopy (AFM, Nano

Scope NS3A system). The conductive and potential images further were measured by conductive atomic force microscopy (C-AFM, Bruker Multimode 8). The focused-ion-beam (FIB)-butted perovskite films with grains and grain boundaries are examined by high resolution transmission electron microscopy (HR-TEM). The crystal structure, absorption properties, elemental compositions and chemical and electron states of perovskite films were analyzed with X-ray diffractometer (XRD, Bruker D8 Advance), ultraviolet-visible (UV-vis, DektakXT), X-ray photoelectron spectroscopy (XPS, AXIS ULTRA DLD, aluminum Kα X-ray radiation) and Fourier transform infrared (FTIR, Thermo) transmittance measurements, respectively. The steady-state of perovskite films were analyzed by photoluminescence (PL) and time-resolved photoluminescence (TRPL) spectra using an Edinburgh Instruments FLS980 fluorescence spectrometer with 460 nm excitation source. GIWAXS measurements were carried out on a Xeuss SAXS/WAXS beamline system based on an X-ray source of Cu Kα with an incident grazing angle of 0.18°. The contact angle measurement was characterized by DSA100 KRÜSS Drop Shape Analyzer, and the ADVANCE software was used to obtain the image and angle information. The elemental depth profiling of perovskite films was analyzed by TOF-SIMS (ION-TOF GmbH).

The performance measurements of all solar cell device without encapsulation were carried out under ambient-air conditions (40-50% humidity and 27-30 °C temperature). The current density-voltage (J-V) curves and performance parameters of PSCs were measured by a Newport solar simulator (Keithley series 2400, ORIEL-SOI3A) with a source meter at 100 mW/cm^2 under AM 1.5 illumination which was calibrated by a silicon reference cell. The dimension of the tested solar cells were 2.5 cm × 2.5 cm. The areas of solar cell performances were examined with 0.0915 cm^2 mask. The external quantum efficiency (EQE) spectrum was measured by using a QE-R instrument from Enlitech, calibrated by a silicon reference cell. The transient photovoltage decay and built-in electric field measurements were performed on an electrochemical workstation (ZAHNER, Germany). For indoor light conditions, SGX T5 5 W LED (3000 K) and fluorescent (FL, 2700 K) were applied as light sources, and the illumination was calibrated to 1000 lux by illuminometer (TES-1330A). Spectrum of the indoor light source (SGX T5 5 W LED 3000 K, and FSL T5 8 W FL 2700 K) was collected using a spectral illuminometer (SPIC-200, Everfine). The indoor light power density was obtained based on light spectrum and luminosity function. The EL and ERE spectra of the perovskite devices were recorded

simultaneously by a commercialized system (XPQY-EQE-350-1100, Guangzhou Xi Pu Optoelectronics Technology Co., Ltd.), which is equipped with an integrated sphere (GPS-4P-SL, Labsphere) and a photodetector array (S7031-1006, Hamamatsu Photonics). Several our cells were sent to an independent national PV industry measurement and testing center (Fujian Metralogy institute) for efficiency certification.

Device characterization

<u>Calculation of non-radiative recombination V_{oc} loss</u>

The non-radiative recombination V_{oc} loss can be calculated by following equation:

$$\Delta V_{OC}^{nonrad} = V_{OC}^{rad} - V_{OC}^{measure} = -\frac{kT}{q}\ln EQE_{EL}$$

where ΔV_{OC}^{nonrad}, ΔV_{OC}^{rad}, $V_{OC}^{measure}$, k, T, q and $\ln EQE_{EL}$ represent the V_{OC} loss of nonradiative recombination, the V_{OC} loss of the sub-band-gap radiative recombination, measured V_{OC}, Kelvin temperature, Boltzmann constant, the elementary charge and the EQE of electroluminescence (EL), respectively. Thus, the passivated device has a lower ΔV_{OC}^{nonrad} of 110.21mV than the pristine device of 142.16 mV.

<u>Calculation of trap density and mobility</u>

The trap density (N_t) can be calculated by following equation:

$$N_t = \frac{2V_{TFL}\varepsilon_r\varepsilon_0}{eL^2}$$

where V_{TFL}, ε_r, ε_0, e and L are the trap-filled limit voltage, relative dielectric constant of the perovskite (35), vacuum permittivity, elementary charge, and thickness of the perovskite layer, respectively. A lower trap density of hole (N_{hole}) of 6.31×10^{15} and electron ($N_{electron}$) of 3.28×10^{15} for the passivated devices was obtained than that of pristine devices ($N_{hole} = 7.26 \times 10^{15}$ and $N_{electron}$=7.26×10^{15}) (Table S7).

The hole (μ_{hole}) and electron ($\mu_{electron}$) mobility can be calculated by following equation:

$$\mu = (8L^3K)/9\varepsilon\varepsilon_0$$

$$J_D = \frac{9\varepsilon\varepsilon_0\mu V^2}{8L^3}$$

$$K = \frac{J_D}{V^2}$$

where ε and ε_0 represent the average relative dielectric constants and vacuum permittivity, J_D and V are the current density and applied voltage, L is the thickness of films, respectively. The passivated devices shows a higher mobility than the pristine based devices (Table S7).

Calculation of ideal factor

The ideal factor (n) can be calculated by following equation:

$$n = \frac{q}{k_B T} \times \frac{dV_{OC}}{d(\ln(L))}$$

Where the k_B is the Boltzmann constant, T is the temperature, q is the electric charge, L and V_{OC} are light intensity and voltage, respectively.

a (28.1°)

Perovskite+DMF+DMSO

b (19.9°)

Perovskite+OAmI+DMF+DMSO+CHCl₃
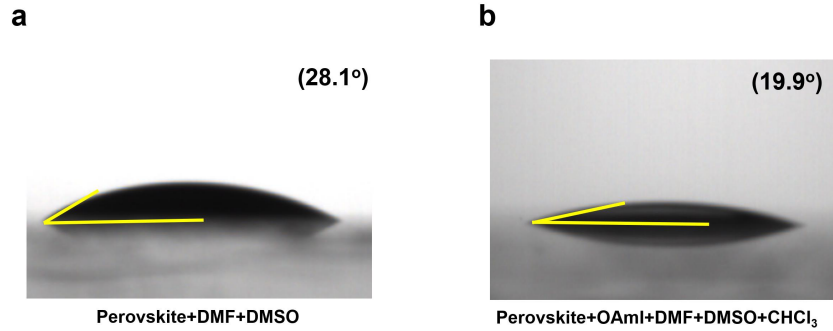
Fig. S1. Results of contact angles. Droplets of (a) perovskite-DMF-DMSO (abbreviated for convenience solution 1) and (b) perovskite-OAmI-DMF-DMSO-CHCl₃ (abbreviated for convenience solution 2) on the ITO/NiO$_x$/PTAA/mp-Al₂O₃ substrate. The contact angle of solution 2 on the ITO/NiO$_x$/PTAA/mp-Al₂O₃ substrate is lower than that of solution 1, indicating an improved interaction of perovskite-OAmI-DMF-DMSO-CHCl₃ ink with the ITO/NiO$_x$/PTAA/mp-Al₂O₃ substrate.[6]
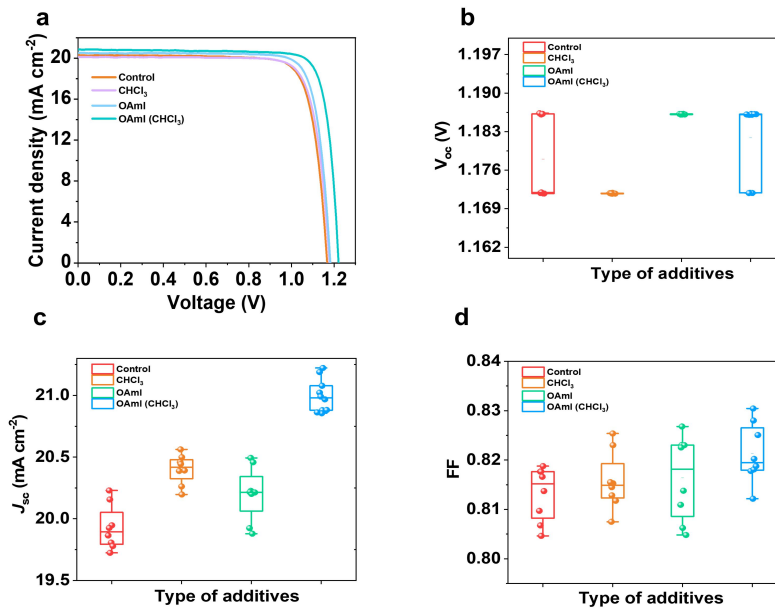
Fig. S2. The effects of different types of additives on solar cell performance. (a) *J-V* curves with reverse scan, and (b to d) the statistics of V_{oc}, J_{sc} and *FF* values for different additives, i.e., pristine perovskite precursor, perovskite precursor incorporating CHCl₃, perovskite precursor incorporating OAmI, and perovskite precursor incorporating OAmI and CHCl₃ (OAmI was pre-dissolved into CHCl₃).
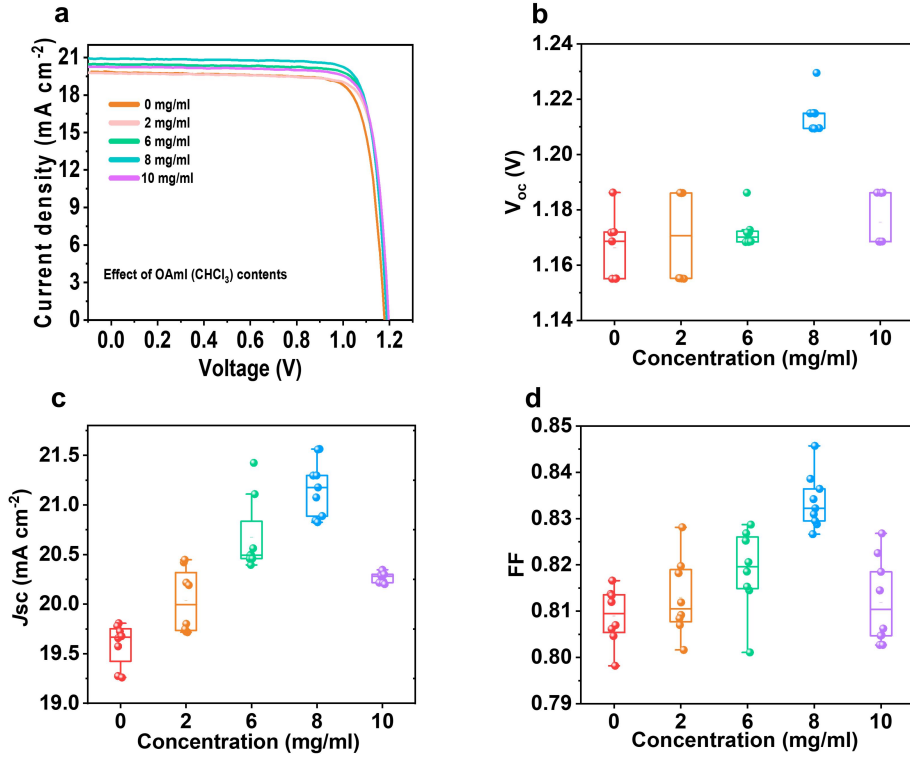
Fig. S3. The effects of OAmI concentration on solar cell performance. (a) *J-V* curves with reverse scan, and (b to d) the statistics of V_{oc}, J_{sc} and *FF* values for different contents of OAmI into CHCl$_3$. Here, the volume ratio of the OAmI solution to perovskite precursor kept at 1:10.
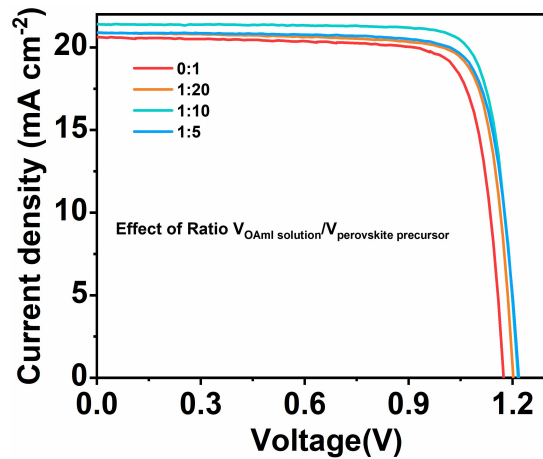

Fig. S4. *J-V* curves with reverse scan for different volume ratio of the OAmI solution to perovskite precursor. Here, the concentration of OAmI in CHCl$_3$ kept at 8 mg/ml.
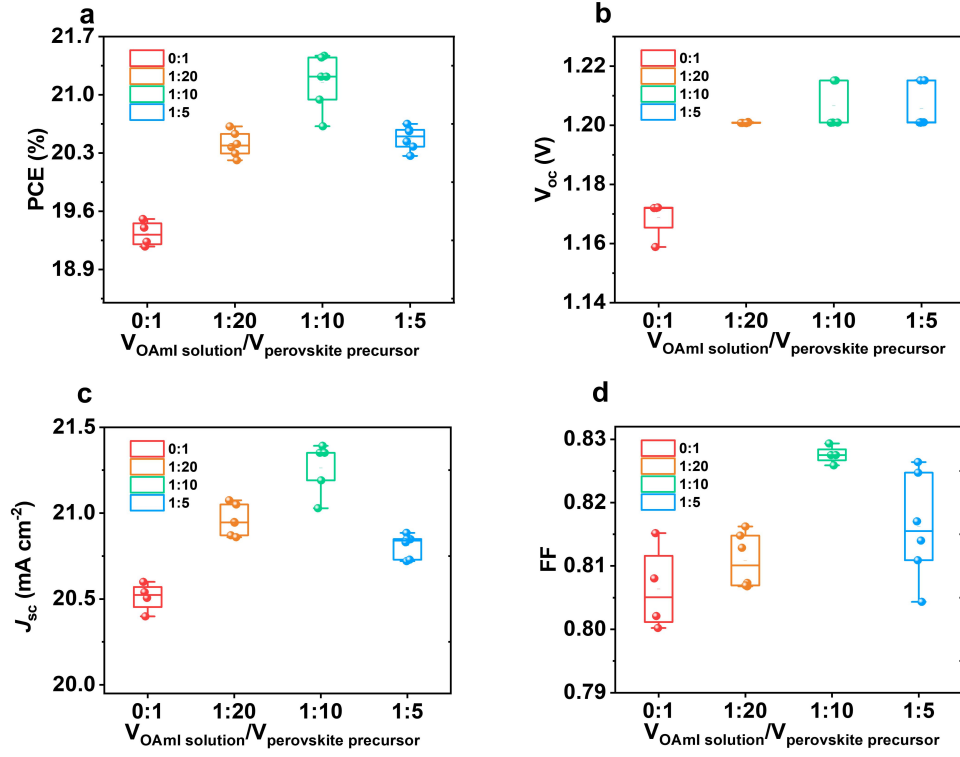
Fig. S5. The effects of OAmI solution contents on solar cell performance. (a to d) The statistics of PCE, V_{oc}, J_{sc} and FF values for different volume ratio of the OAmI solution to perovskite precursor. Here, the concentration of OAmI in CHCl$_3$ kept at 8 mg/ml.

福建省计量科学研究院
FUJIAN METROLOGY INSTITUTE
（国家光伏产业计量测试中心）
National PV Industry Measurement and Testing Center

报告编号：22Q3-00217
Report No.

检测结果/说明：
Results of Test and Additional Explanation.

1   Standard Test Condition (STC)：Total Irradiance：1000 W/m²

Temperature：25.0 ℃

Spectral Distribution：AM1.5G

2   Measurement Data and I-V/P-V Curves under STC

Forward Scan

I_{sc} (mA)	V_{oc} (V)	I_{MPP} (mA)	V_{MPP} (V)	P_{MPP} (mW)	FF (%)	η (%)
1.833	1.248	1.703	1.101	1.875	81.96	20.49

Reverse Scan

I_{sc} (mA)	V_{oc} (V)	I_{MPP} (mA)	V_{MPP} (V)	P_{MPP} (mW)	FF (%)	η (%)
1.827	1.248	1.727	1.101	1.901	83.37	20.77

Mismatch Factor: 1.013
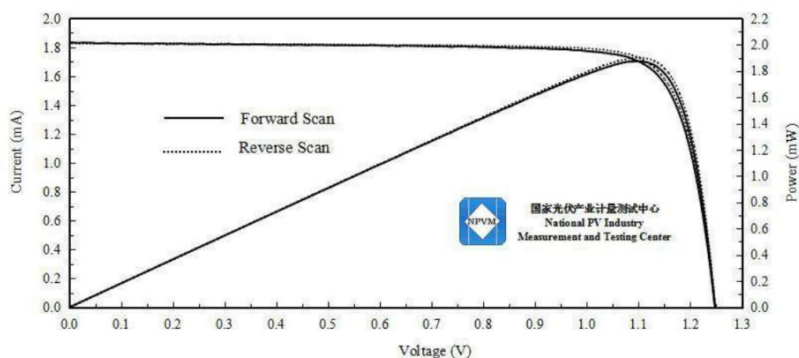
Figure 1. I-V and P-V characteristic curves of the measured sample under STC

检测报告续页专用
Continued page of test report

Fig. S6. The certification photovoltaic parameters and corresponding *I-V* curves report of a sister cell under one-sun illumination by Chinese national PV industry measurement and testing center.

报告编号：22Q3-00217
Report No.

检测结果/说明：
Results of Test and Additional Explanation.

3   Measurement Data and Curves for MPPT under STC

η (%)	20.42
P_{MPP} (mW)	1.869
I_{MPP} (mA)	1.705
V_{MPP} (V)	1.096

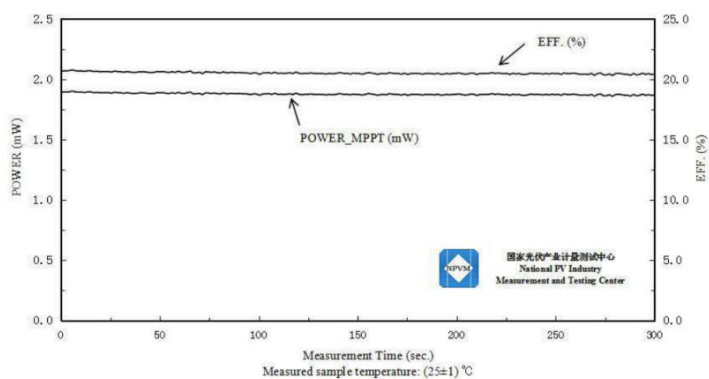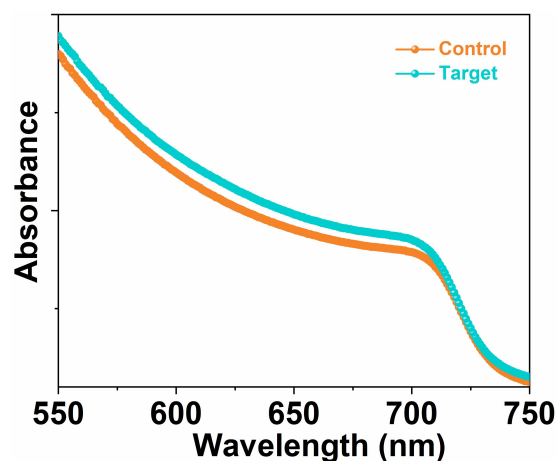Note: Measurement data for MPPT under STC in the above table was acquired at 300 sec..

Figure 2. Measurement curves of the measured sample for MPPT

检测报告续页专用
Continued page of test report

Fig. S7. The certification MPPT report of a sister cell under one-sun illumination by Chinese national PV industry measurement and testing center.

Fig. S8. UV-vis spectra of control and target perovskite films. The light absorbance in passivated films is better than that of pristine perovskite films.
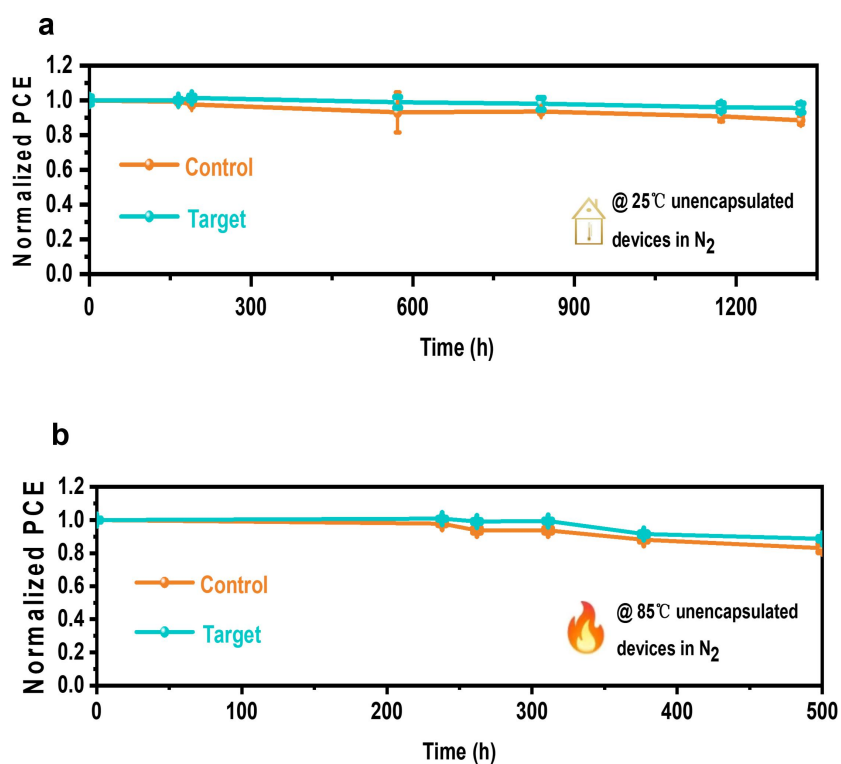

Fig. S9. (a to b) Storage stability and thermal stability under N_2 atmosphere for control and target cells. Here, the concentration of OAmI in $CHCl_3$ and volume ratio of the OAmI solution to perovskite precursor kept at 8 mg/ml and 1:10, respectively. The target cells showed better storage and thermal stability than pristine cells.
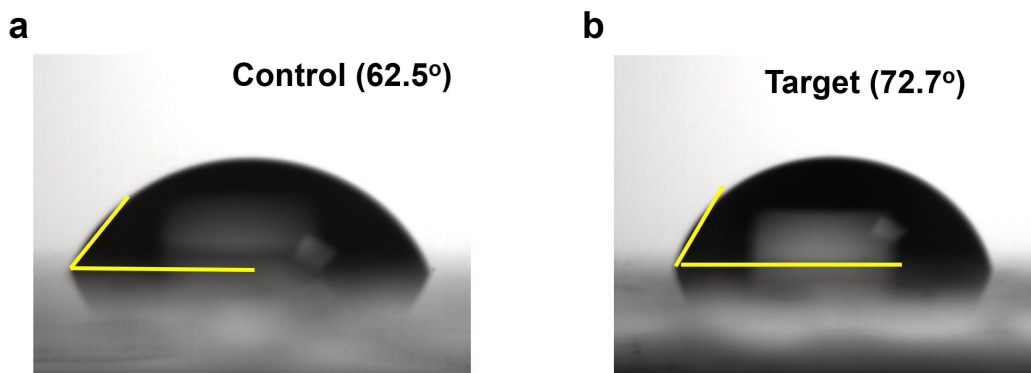
Fig. S10. (a to b) Contact angle measurement of control and target perovskite films. The contact angle of target perovskite film is higher than that of control perovskite film, indicating more hydrophobic property.
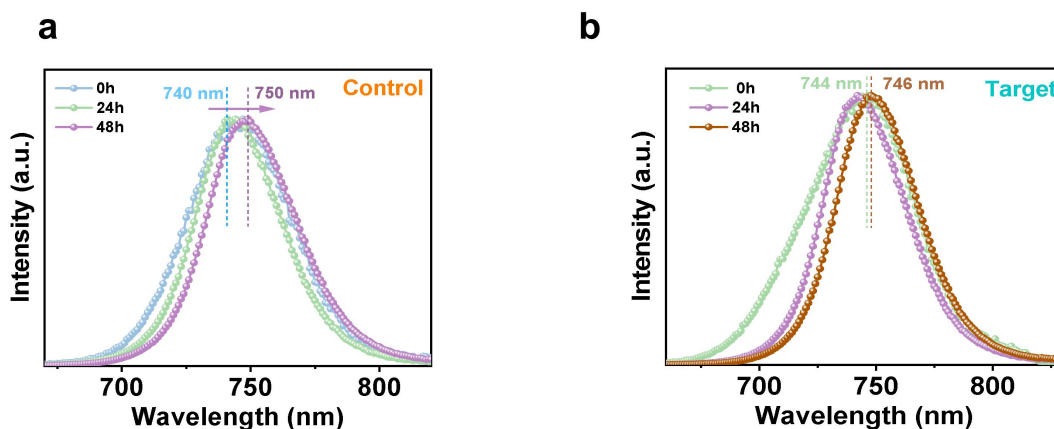

Fig. S11. (a to b) Halide segregation study of control and target perovskite films treated with continuous one-Sun illumination by PL spectra measurement (Note that each sample was treated under one-Sun illumination at different times before PL spectra measurement. The excitation wavelength for PL measurement is 450 nm). Compared to target perovskite films, the PL spectra of control perovskite films substantially shifted to a long wavelength from approximately 740 nm to 750 nm as the light illumination time increases, indicating the presence of halide segregation.
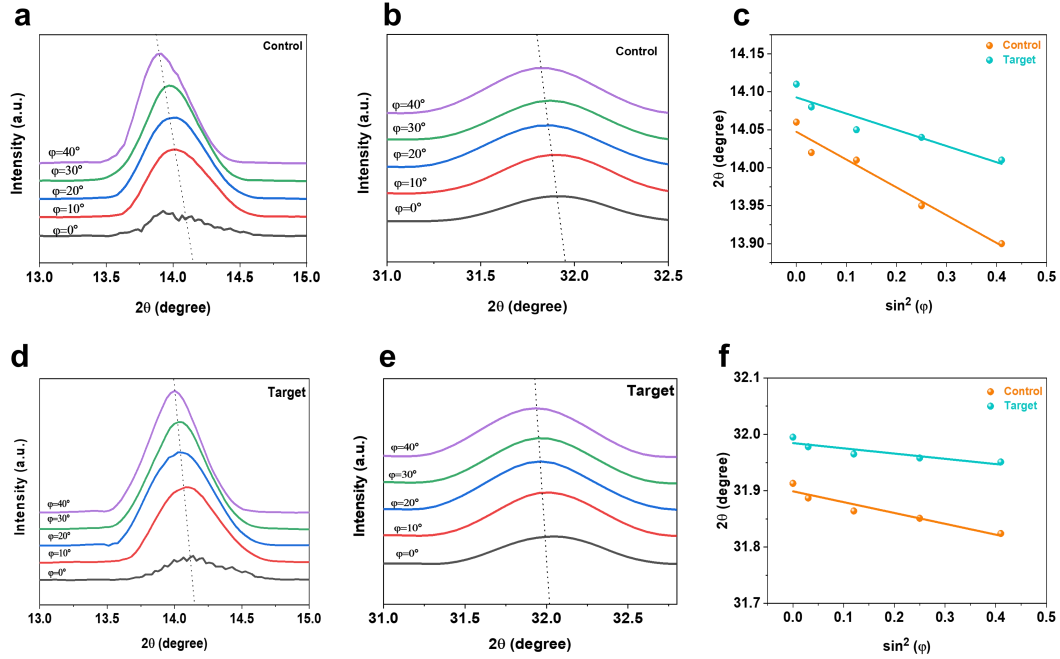
Fig. S12. (a, d) and (b, e) GIXRD spectra at different tilt angles for 2θ at 14.12° and 31.58°, and (c, f) corresponding linear fit of residual strain as a function of $\sin^2(\varphi)$ for control and target perovskite films, respectively. The linear fit curves for 2θ position as a function of $\sin^2(\varphi)$ in the target perovskite films have slower slopes than that of the control 3D perovskite films (Fig. 2h), indicating efficient suppression of the residual stress and lattice distortion.
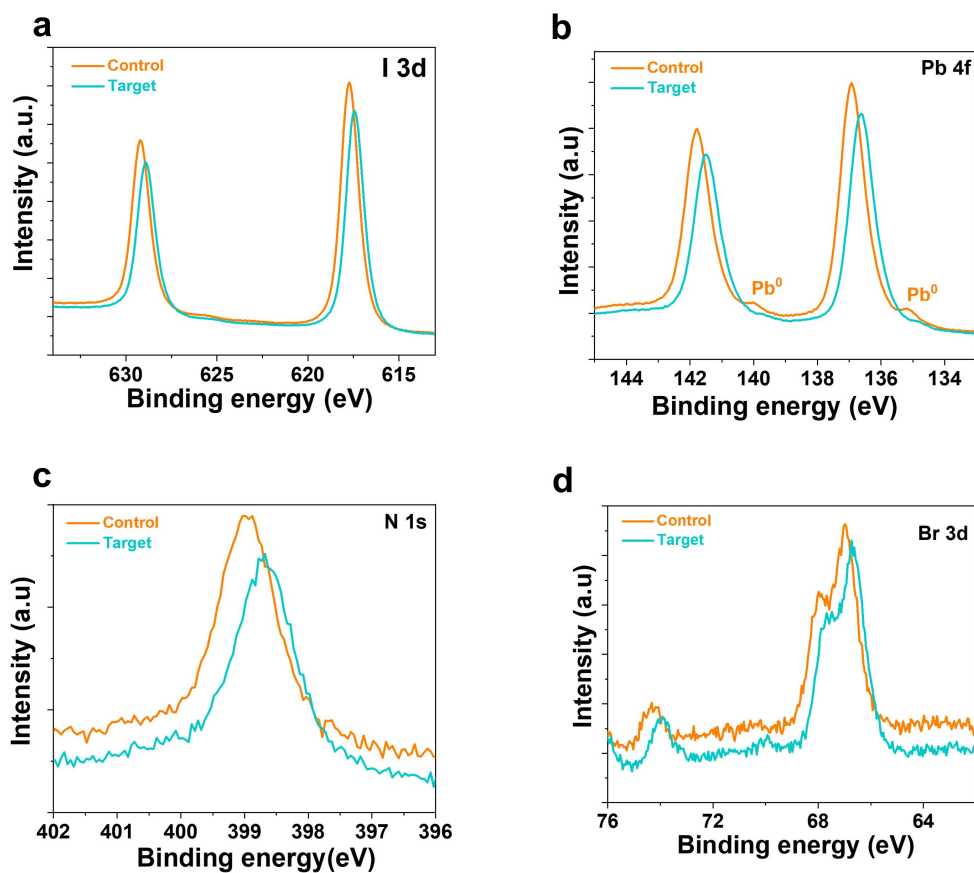
Fig. S13. (a to d) XPS spectra of control and target perovskite films. The core levels of I 3d, Pb 4f, N 1s and Br 3d) present a substantial shift toward lower binding energy, indicating the presence of chemical interaction between OAm$^+$ and perovskite molecules. The metallic Pb^0 can be remarkably suppressed in the target perovskite film.
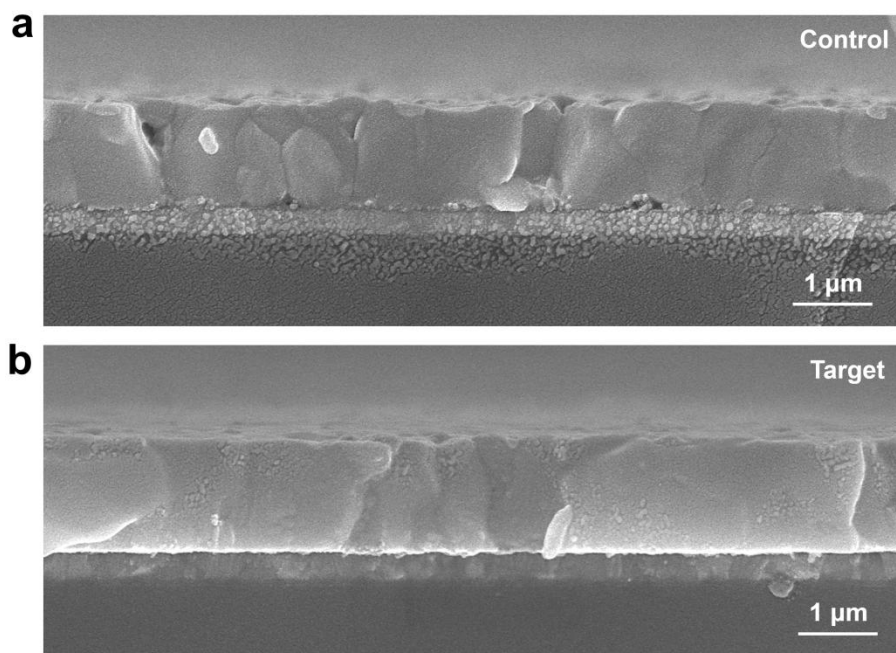
Fig. S14. (a to b) Cross-view SEM images of control and target perovskite films.
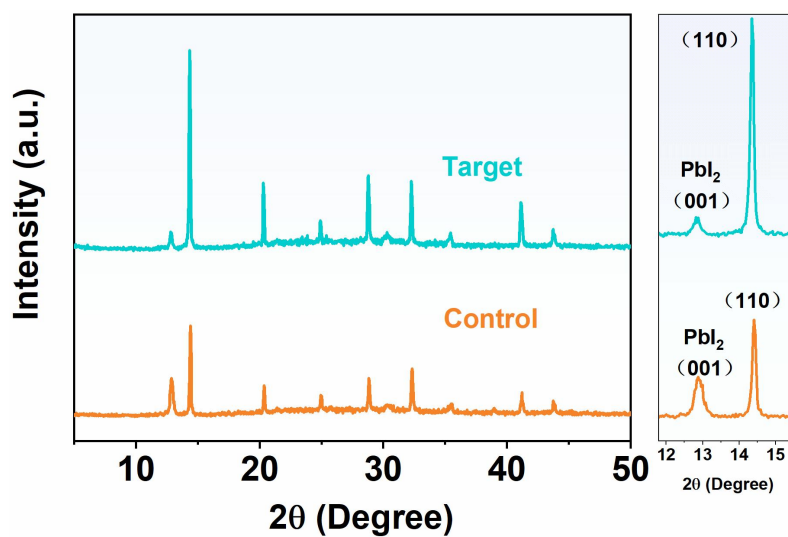

Fig. S15. XRD patterns of control and target perovskite films. The crystallization quality in target films is better than that of control perovskite films. The lower intensity of PbI_2 is attributed to the formation of 2D perovskites.
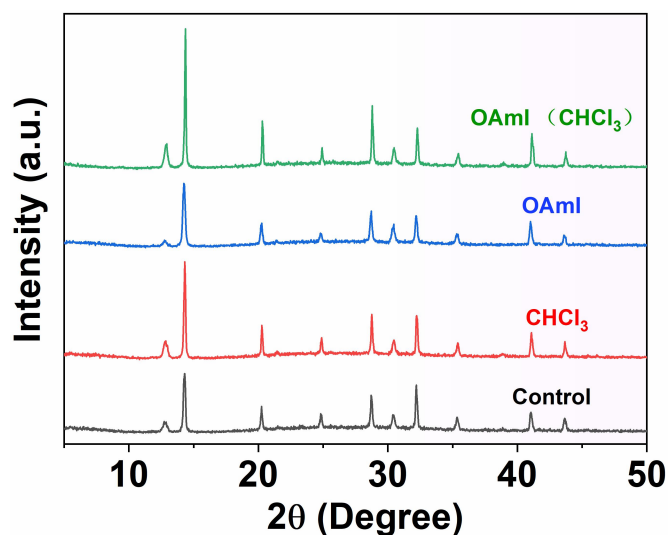
Fig. S16. XRD patterns of WBG-perovskites based on different types of additives. It is observed that OAmI acts as a passivation site of lead iodide defects for 2D perovskite formation, and CHCl₃ is beneficial for the crystallinity of perovskites.

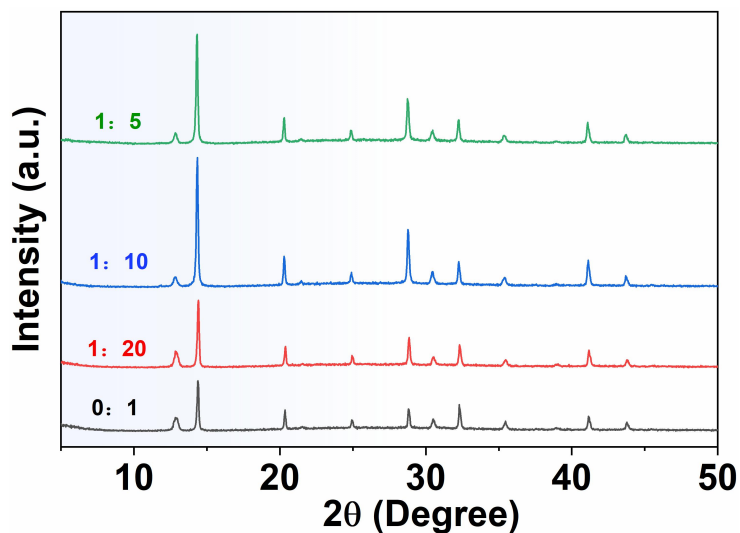**Fig. S17**. XRD patterns of WBG-perovskites based on different different volume ratios of OAmI solution to perovskite precursors. The results show that the preparation of perovskite films with an ideal ratio is beneficial for high crystallinity.
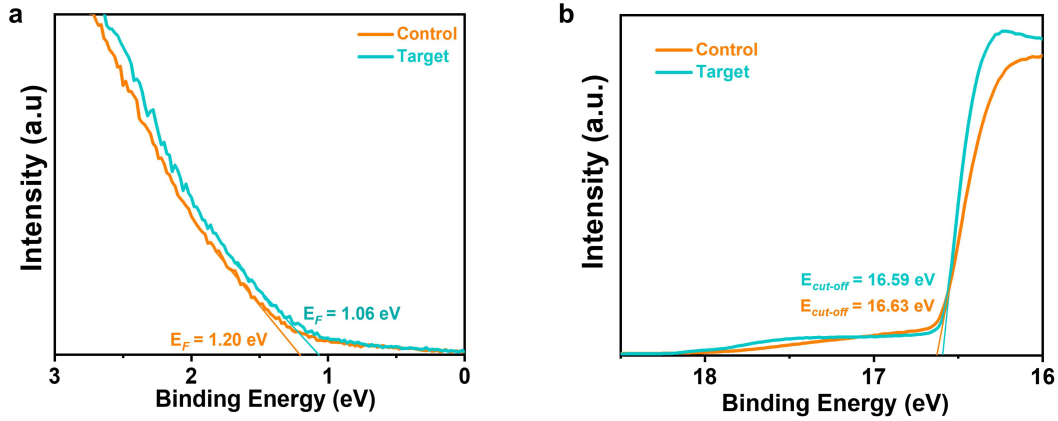
Fig. S18. (a to b) UPS of the Fermi level (E_F) energy and corresponding cutoff ($E_{cut\text{-}off}$) regions of control and target perovskite films. $VB_{Control}$ = -5.79 eV, $CB_{Control}$ = -4.08 eV; VB_{Target} = -5.69 eV, CB_{Target} = -3.98 eV.
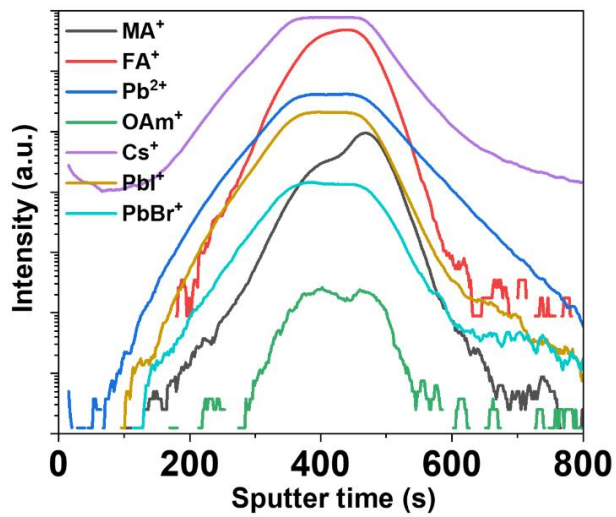
Fig. S19. TOF-SIMS depth profiles of target WBG-perovskite film. The OAm^+ ions are well distributed throughout the region of WBG-perovskite active layer. No halide ion migration was observed.
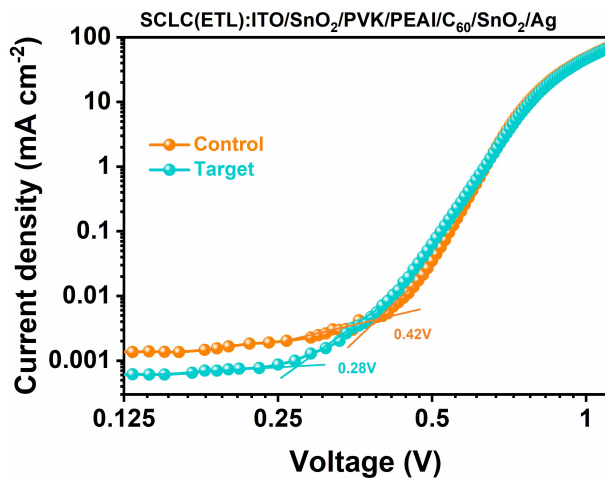
Fig. S20. Space-charge-limited-current (SCLC) curves of electron-only devices for control and target WBG-perovskite films.
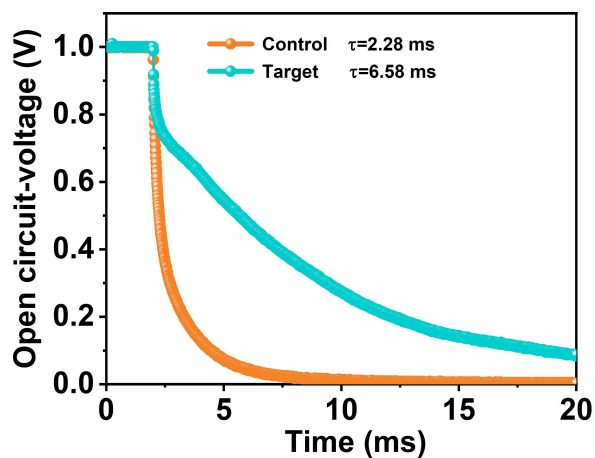
Fig. S21. Open-circuit voltage decay (OCVD) response time for control and target PSCs. The OCVD response time of target perovskite device is longer than that of control perovskite device.
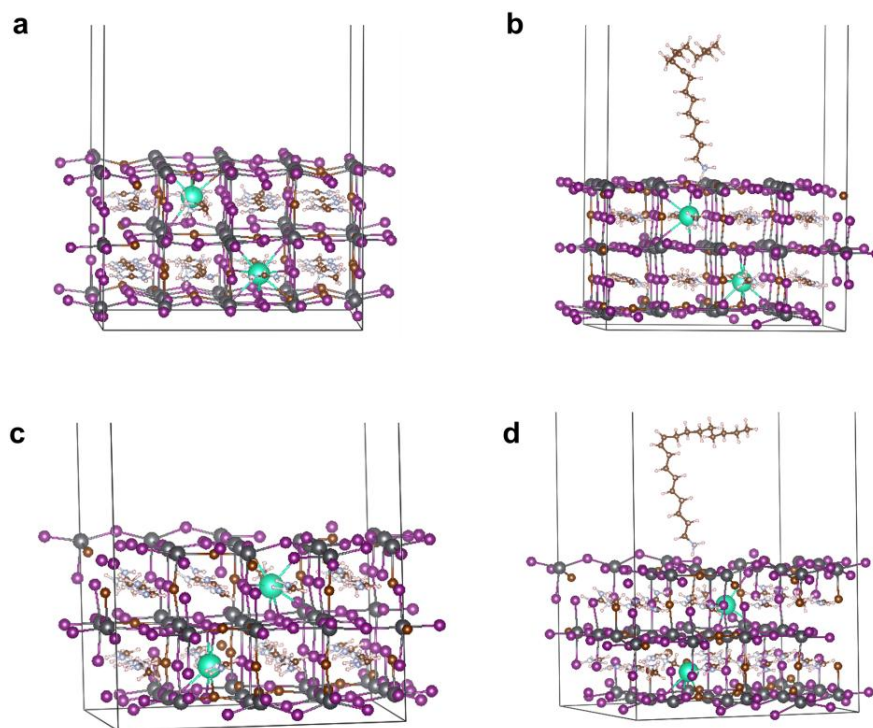
Fig. S22. (a to d) The density functional theory (DFT) calculations of FAMAPbI$_3$ (001), FAMAPbI$_3$-OAm, Vacancy-FAMAPbI$_3$ (001) and Vacancy-FAMAPbI$_3$ (001)-OAmI.
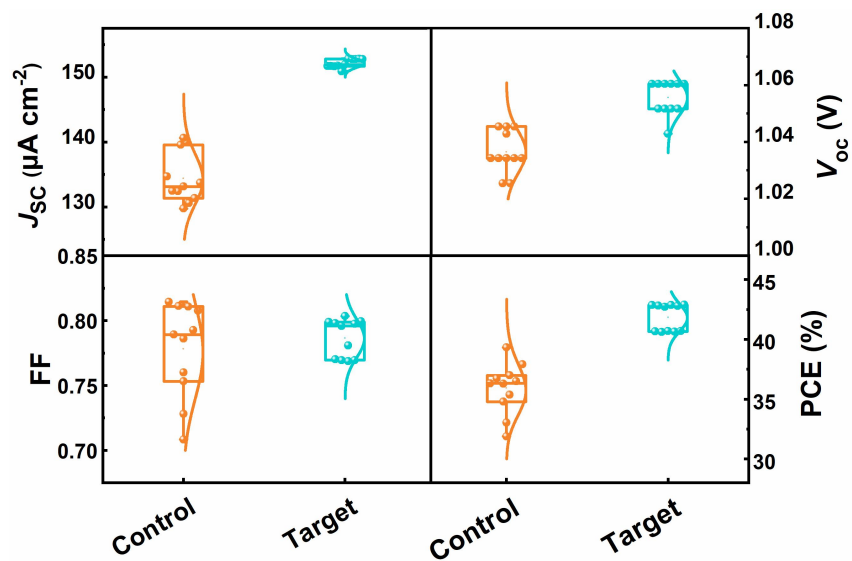
Fig. S23. The statistics of J_{sc}, V_{oc}, FF and PCE values for control and target PSCs under LED illumination (1000 lux, 3000 K). The target devices show excellent reproducibility.
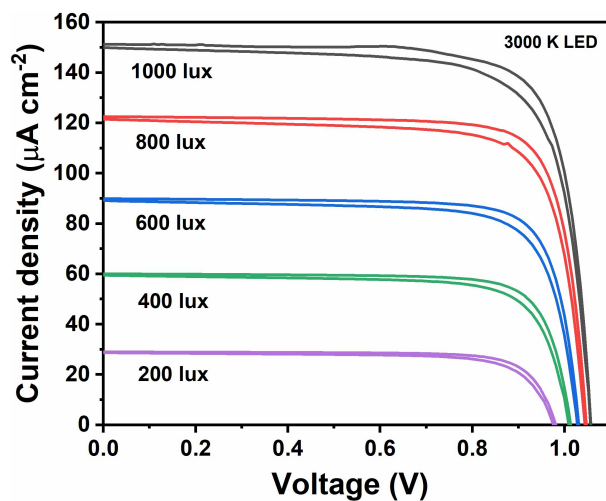
Fig. S24. *J-V* curves of champion target WBG-PSCs at different light density from 200 to 1000 lux illumination.
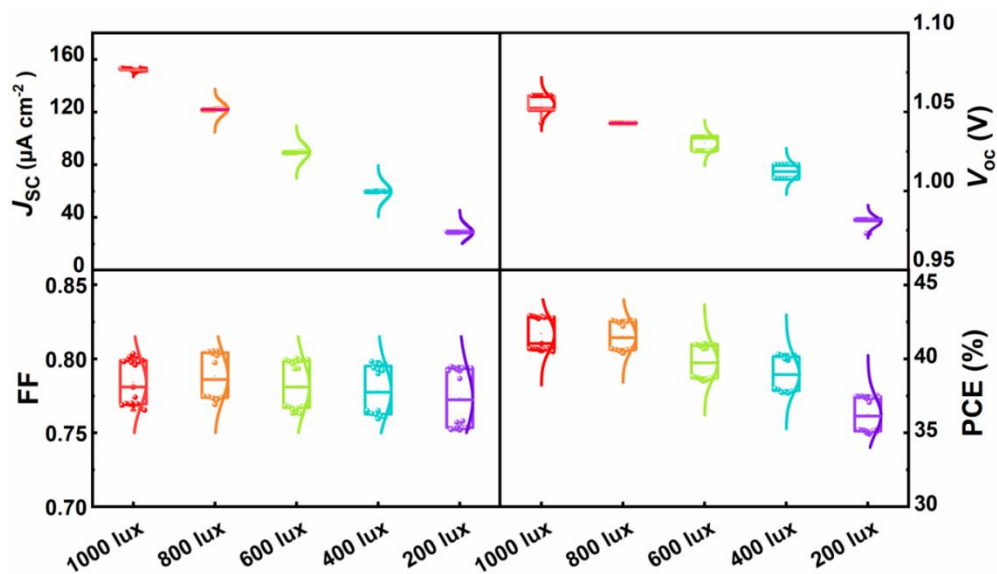
Fig. S25. The statistics of J_{sc}, V_{oc}, FF and PCE values for target WBG-PSCs under LED illumination with different light density from 200 to 1000 lux (3000 K).
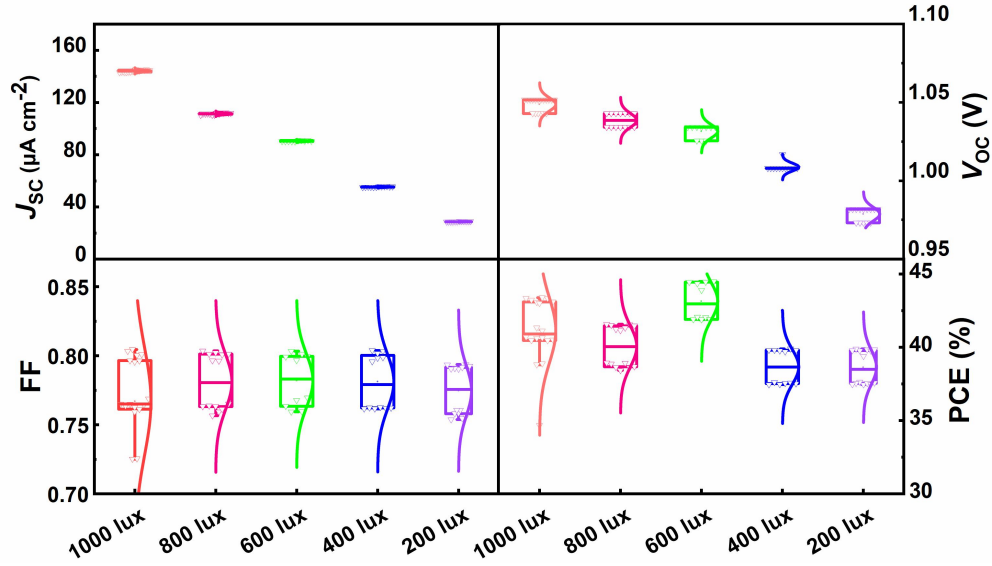
Fig. S26. The statistics of J_{sc}, V_{oc}, FF and PCE values for target WBG-PSCs under fluorescent (FL) illumination with different light density from 200 to 1000 lux (2700 K).
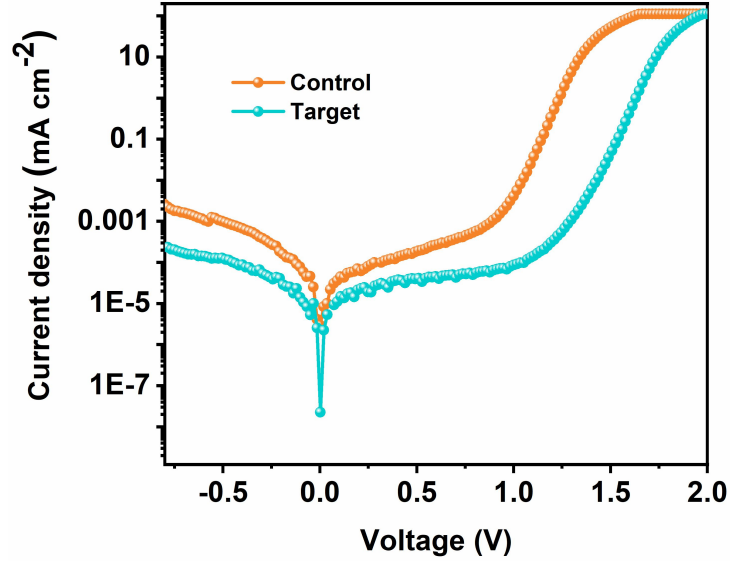
Fig. S27. Dark J-V curves of control and target devices.
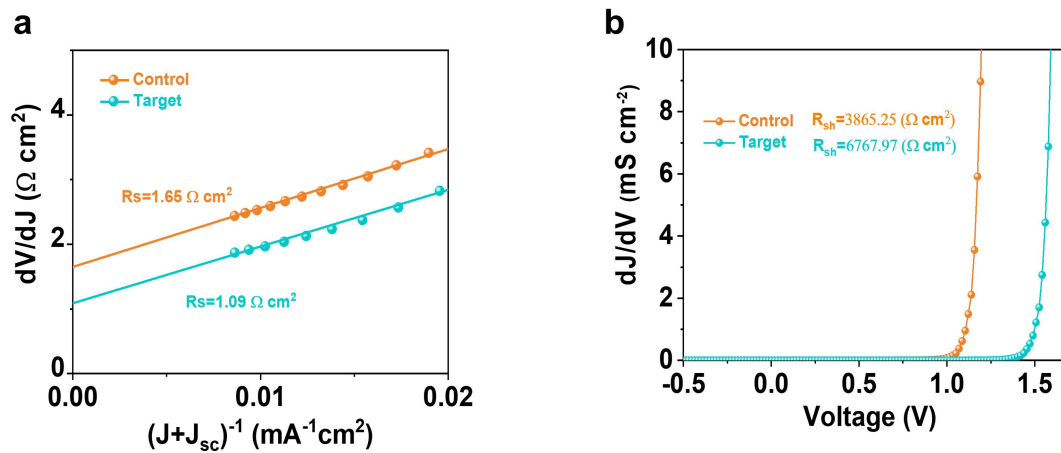
Fig. S28. (a) The *dV/dJ* with the fit used to determine R_s, and (b) The *dJ/dV* with the fit used to determine R_{sh} for control and target WBG-PSCs. Compared to control WBG-PSCs, the target WBG-PSCs have lower R_s but higher R_{sh}.

报告编号：22Q3-00223
Report No.

检测结果/说明：
Results of Test and additional explanation.

1   Standard Test Condition (STC)：Total Illuminance：1000 lux

Temperature：25.0 ℃

Spectral Distribution：indoor light
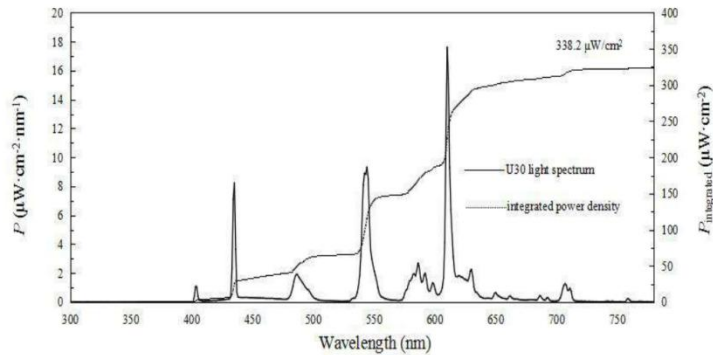
Figure 1. Spectral distribution of indoor lights and the corresponding integrated power density

2   Measurement Data and I-V/P-V Curves of Indoor Light under STC

Indoor Light	Direction	I_{sc} (mA)	V_{oc} (V)	I_{MPP} (mA)	V_{MPP} (V)	P_{MPP} (mW)	FF (%)	η (%)
U30	Forward	0.01563	1.059	0.01446	0.9182	0.01328	80.23	42.91
	Reverse	0.01574	1.069	0.01492	0.9276	0.01384	82.25	44.72

检测报告续页专用
Continued page of test report

Fig. S29. The certification indoor photovoltaic parameters report of a sister cell under U30 light by Chinese national PV industry measurement and testing center.

24

报告编号：22Q3-00223
Report No.

检测结果/说明：
Results of Test and additional explanation.
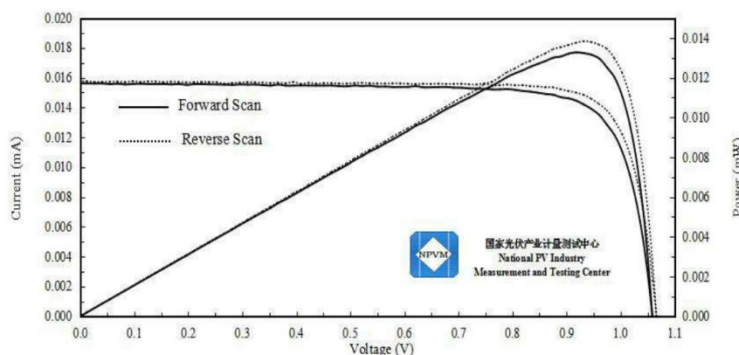
Figure 2. I-V and P-V characteristic curves of the measured sample with indoor light of U30 under STC

3   Pictures of the Measured Sample
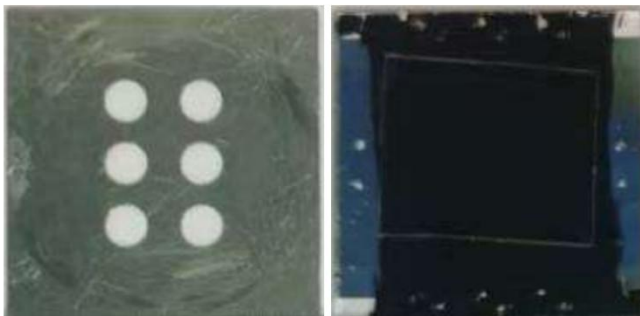
Figure 3. Mask used during test and obverse side of the sample

检测报告续页专用
Continued page of test report

Fig. S30. The certification *I-V* curves report of a sister cell under U30 light by Chinese national PV industry measurement and testing center.
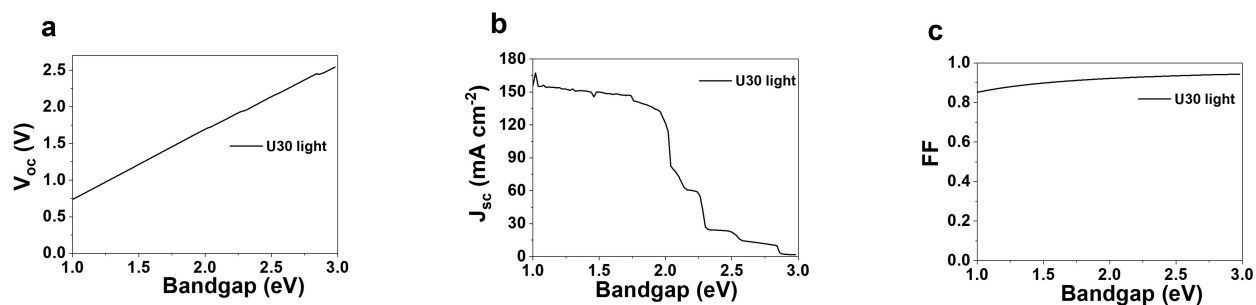
Fig. S31. (a to c) The *S-Q* limit of V_{oc}, J_{sc} and FF of an ideal photovoltaic device as a function of band-gap energy under the U30 light. According to U30 light spectrum (Fig. 5c), the values of *S-Q* limit of V_{oc}, J_{sc}, FF and PCE were calculated.

Table S1. Binding energy for different perovskite-solvent adducts.

Perovskite-solvent adducts	E_{total} (Ha)	E1 (Ha)	E2 (Ha)	ΔE (eV)
Perovskite-DMF-DMSO	-553852.34643	-553051.11709	-801.19108	-1.04
Perovskite-DMF-DMSO-CHCl$_3$	-555271.25343	-553051.16210	-2220.01077	-2.19
Perovskite-OAmI-DMF-DMSO	-554615.08504	-553051.16351	-1563.78060	-3.83
Perovskite-OAmI-DMF-DMSO-CHCl$_3$	-556033.94032	-553051.15784	-2982.61844	-4.46

Table S2. Photovoltaic parameters of WBG-PSCs under one sun illumination based on different contents of OAmI+CHCl$_3$.

Contents of OAmI+CHCl$_3$	V_{oc} (V)	J_{sc} (mA cm^{-2})	FF (%)	PCE (%)
0 mg/ml	1.171	19.78	81.37	18.86
2 mg/ml	1.186	19.72	82.81	19.37
6 mg/ml	1.186	20.44	83.02	20.13
8 mg/ml	1.186	20.88	82.80	20.51
10 mg/ml	1.186	20.23	82.68	19.84

Table S3. Photovoltaic parameters of passivated-based WBG-PSCs for different volume ratio of OAmI+CHCl$_3$ solution and perovskite precursor, measured under one sun illumination.

Ratio of $V_{\text{OAmI solution}} : V_{\text{perovskite precursor}}$	V_{oc} (V)	J_{sc} (mA cm^{-2})	FF (%)	PCE (%)
0:1	1.17	20.60	80.80	19.51
1:20	1.22	20.88	81.09	20.58
1:10	1.22	21.39	82.59	21.47
1:5	1.20	20.87	81.29	20.37

Table S4. Photovoltaic parameters of champion control and target WBG-PSCs under one sun illumination.

Device	Scan direction	V_{oc} (V)	J_{sc} (mA cm^{-2})	FF (%)	PCE (%)
Control	Reverse	1.17	20.82	82.58	20.37
	Forward	1.17	20.77	81.70	19.96
Target	Reverse	1.23	21.56	82.88	21.97
	Forward	1.22	21.56	82.95	21.73

Table S5. Reported efficiencies of WBG-perovskite solar cells (E_g=1.65 eV~1.80 eV) under one sun illumination.

WBG-Perovskites	E_g (eV)	V_{oc} (V)	J_{sc} (mA/cm^2)	FF (%)	PCE (%)	REF.
$Cs_xFA_yMA_{1-(x+y)}Pb(I,Br)_3$	1.65	1.14	23.19	80.60	21.31	7
$Cs_{0.1}FA_{0.2}MA_{0.7}Pb(I_{0.85}Br_{0.15})_3$	1.65	1.23	21.20	83.80	21.90	8
$FAMACsPb(I_{0.8}Br_{0.2})_3$	1.67	1.19	23.06	79.32	21.85	9
$Cs_{0.05}FA_{0.8}MA_{0.15}Pb(I_{0.75}Br_{0.25})_3$	1.68	1.22	20.60	81.00	20.20	10
$Cs_{0.05}(FA_{0.77}MA_{0.23})_{0.95}Pb(I_{0.77}Br_{0.23})_3$	1.68	1.22	20.70	82.00	20.80	11
$Cs_{0.05}FA_{0.8}MA_{0.15}Pb(I_{0.755}Br_{0.255})_3$	1.69	1.22	20.58	81.10	20.46	12
$Cs_{0.17}FA_{0.83}Pb(I_{0.6}Br_{0.4})_3$	1.72	1.31	19.30	78.00	19.80	13
$FAMACsPb(I_{0.7}Br_{0.3})_3$	1.73	1.30	19.68	83.27	21.30	14
$FA_{0.8}Cs_{0.2}Pb(I_{0.7}Br_{0.3})_3$	1.75	1.21	19.30	86.50	20.20	15
$CH_3NH_3Pb(I_{0.8}Br_{0.2})_3$	1.72	1.35	17.20	81.20	18.90	16
$FA_{0.78}Cs_{0.22}Pb(Br_{0.3}I_{0.7})_3$	1.80	1.36	18.11	81.50	20.00	17
$Cs_{0.05}FA_{0.70}MA_{0.25}PbI_{2.25}Br_{0.75}$	**1.71**	**1.23**	**21.56**	**82.88**	**21.97**	**This work**

Table S6. The values of TRPL obtained by fitting curves (Fig. 4b) for control and target WBG-perovskite films.

Device configurations	τ_1 (ns)	A_1	τ_2 (ns)	A_2	Average (ns)
Control	109.09	7.33	1410.88	92.67	1315.46
Target	99.70	2.60	2410.42	97.40	2350.34

Table S7. The trap density and charge mobilities of the hole-only and electron-only devices based on control and target perovskite films.

Device	Trap density (cm^{-3})		Mobility ($cm^2v^{-1}s^{-1}$)	
	Hole-only device	Electron-only device	Hole-only device	Electron-only device
Control	7.26×10^{15}	4.91×10^{15}	6.55×10^{-2}	9.36×10^{-2}
Target	6.31×10^{15}	3.28×10^{15}	8.92×10^{-2}	9.38×10^{-2}

Table S8. Defect formation energy of FAMAPbI$_3$ and FAMAPbI$_3$-OAm.

	E(Ha)
FAMAPbI$_3$ (001)	-1707581.69877
Vacancy-FAMAPbI$_3$ (001)	-1678312.81041
FA	-150.48070
MA	-96.34710
Pb	-19527.90651
I	-6920.16226
Br	-2573.90820

(1) Defect formation energy of FAMAPbI$_3$:

$\Delta E1=27.212 \times (E_{Vacancy-FAMAPbI3\ (0\ 0\ 1)} + E_{FA} +E_{MA}+E_I+E_{Br}-E_{FAMAPbI3\ (0\ 0\ 1)})=0.08359\times27.212=2.27$ eV

	E(Ha)
FAMAPbI$_3$ (001)-OAmI	-1708344.50520
Vacancy-FAMAPbI$_3$ (001)-OAmI	-1679075.55377
FA	-150.48070
MA	-96.34710
Pb	-19527.90651
I	-6920.16226
Br	-2573.90820

(2) Defect formation energy of FAMAPbI$_3$-OAmI:c

$\Delta E=27.212\times(E_{Vacancy-FAMAPbI3(001)-OAmI}+E_{FA}+E_{MA}+E_I+E_{Br}-E_{FAMAPbI3(001)-OAm})=0.14666\times27.212$ $=3.99$ eV

Table S9. Photovoltaic parameters of champion control and target WBG-PSCs under LED illumination (1000 lux, 3000 K).

Device	Scan direction	V_{oc} (V)	J_{sc} (µA cm^{-2})	FF (%)	PCE (%)
Control	Reverse	1.04	135.57	79	37.53
	Forward	1.03	134.74	77	35.36
Target	Reverse	1.06	151.93	81	42.86
	Forward	1.04	150.89	79	40.74

Table S10. Photovoltaic parameters of champion target WBG-PSCs under LED illumination with different light density (3000 K).

Illumination condition	P_{in} (µW/cm^{-2})	Scan direction	V_{oc} (V)	J_{sc} (µA cm^{-2})	FF (%)	PCE (%)	P_{out} (µW/cm^{-2})
1000	301.9	Reverse	1.06	151.93	80.34	42.86	129.38
		Forward	1.04	150.89	78.09	40.74	123.00
800	241.5	Reverse	1.04	122.50	80.53	42.76	103.27
		Forward	1.04	121.57	77.45	40.84	98.62
600	181.2	Reverse	1.03	89.85	79.95	41.09	74.43
		Forward	1.03	89.12	76.87	38.75	70.22
400	120.8	Reverse	1.02	60.00	79.62	40.31	48.69
		Forward	1.01	59.48	76.30	37.66	45.50
200	60.4	Reverse	0.98	29.05	79.37	37.48	22.64
		Forward	0.98	28.74	75.35	35.50	21.44

Table S11. Photovoltaic parameters of champion target WBG-PSCs under FL illumination with different light density (2700 K).

Illumination condition	P_{in} (μW/cm^{-2})	Scan direction	V_{oc} (V)	J_{sc} (μA cm^{-2})	FF (%)	PCE (%)	P_{out} (μW/cm^{-2})
1000	281.8	Reverse	1.052	144.50	80.46	43.43	122.37
		Forward	1.043	143.56	76.49	40.65	114.54
800	225.5	Reverse	1.043	112.39	80.12	41.64	93.90
		Forward	1.034	111.44	76.13	38.89	87.69
600	169.2	Reverse	1.034	90.67	79.96	44.33	75.00
		Forward	1.026	89.72	76.96	41.89	70.88
400	112.8	Reverse	1.017	55.72	79.57	39.99	45.11
		Forward	1.008	54.778	76.21	37.30	42.08
200	56.4	Reverse	0.982	29.28	79.05	40.27	22.71
		Forward	0.973	28.33	76.06	37.20	20.98

Table S12. Reported indoor efficiency of indoor perovskite solar cells under different illumination conditions.

Perovskites	E_g (eV)	Illumination conditions	V_{oc} (V)	FF (%)	i-PCE (%)	REF.
$MAPbI_{3-x}Cl_x$	~1.60	FL, 1000 lux	0.85	77.0	27.4	18
$MAPbI_3$	~1.60	LED, 400 lux	0.90	72.7	26.9	19
$MAPbI_3$	~1.63	FL, 1000 lux	0.87	75.0	35.2	20
$MAPbI_{2-x}BrCl_x$	1.80	FL, 1000 lux	1.03	76.8	36.2	21
$(FAPbI_3)_{0.97}(MAPbBr_3)_{0.03}$	1.59	LED, 824.5 lux	1.00	79.5	40.1	22
$Cs_{0.17}FA_{0.83}Pb(I_{0.7}Br_{0.3})_3$	1.72	LED, 1000 lux	0.90	82.5	30.9	23
$Cs_{0.05}MA_{0.05}FA_{0.90}PbI_{2.85}Br_{0.15}$	1.54	LED, 1000 lux	1.06	81.5	41.23	24
$Cs_{0.17}FA_{0.83}PbI_{1.8}Br_{1.2}$	~1.77	TL84, 1000 lux	6.43	72.9	36.36 (module)	25
$FAPbI_3$	~1.55	LED, 1062 lux	0.92	77.1	31.85	26
$Cs_{0.05}FA_{0.70}MA_{0.25}PbI_{2.25}Br_{0.75}$	**~1.71**	**U30, 1000 lux**	**1.07**	**82.3**	**44.72 (certified)**	**This work**

References

1. G. Lippert, J. Hutter and M. Parrinello, *Mol. Phys.*, 2010, **92**, 477-488.

2. J. VandeVondele and J. Hutter, *J. Chem. Phys.*, 2007, **127**, 114105.

3. Y. Wang, H. Ju, T. Mahmoudi, C. Liu, C. Zhang, S. Wu, Y. Yang, Z. Wang, J. Hu, F. Guo, Y.-B. Hahn and Y. Mai, *Nano Energy*, 2021, **88**, 106285.

4. B. Yu, F. Tang, Y. Yang, J. Huang, S. Wu, F. Lu, W. Duan, A. Lambertz, K. Ding and Y. Mai, *Adv. Mater.*, 2023, **35**, 2202447.

5. L. Liu, Y. Ma, Y. Wang, Q. Ma, Z. Wang, Z. Yang, M. Wan, T. Mahmoudi, Y.-B. Hahn and Y. Mai, *Nano-Micro Lett.*, 2023, **5**, 117.

6. F. H. Isikgor, A. S. Subbiah, M. K. Eswaran, C. T. Howells, A. Babayigit, M. D. Bastiani, E. Yengel, J. Liu, F. Furlan, G. T. Harrison, S. Zhumagali, J. I. Khan, F. Laquai, T. D. Anthopoulos, I. McCulloch, U. Schwingenschlögl and S. D. Wolf, *Nano Energy*, 2021, **81**, 81.

7. L. Mao, T. Yang, H. Zhang, J. Shi, Y. Hu, P. Zeng, F. Li, J. Gong, X. Fang, Y. Sun, X. Liu, J. Du, A. Han, L. Zhang, W. Liu, F. Meng, X. Cui, Z. Liu and M. Liu, *Adv. Mater.*, 2022, **34**, 2206193.

8. G. Yang, Z. Ni, Z. J. Yu, B. W. Larson, Z. Yu, B. Chen, A. Alasfour, X. Xiao, J. M. Luther, Z. C. Holman and J. Huang, *Nat. Photon.*, 2022, **16**, 588-594.

9. T. Huang, S. Tan, S. Nuryyeva, I. Yavuz, F. Babbe, Y. Zhao, M. A. Samie, M. H. Weber, R. Wang, K. N. Houk, C. M. Sutter-fella and Y. Yang, *Sci. Adv.*, 2021, **7**, eabj1799.

10. J. Liu, E. Aydin, J. Yin, M. D. Bastiani, F. H. Isikgor, A. U. Rehman, E. Yengel, E. Ugur, G. T. Harrison, M. Wang, Y. Gao, J. I. Khan, M. Babics, T. G. Allen, A. S. Subbiah, K. Zhu, X. Zheng, W. Yan, F. Xu, M. F. Salvador, O. M. Bakr, T. D. Anthopoulos, M. Lanza, O. F. Mohammed, F. Laquai and S. D. Wolf, *Joule,* 2021, **5**, 3169-3186.

11. A. Al-Ashouri, E. Köhnen, B. Li, A. Magomedov, H. Hempel, P. Caprioglio, et al, *Science*, 2020, **370**, 1300-1309.

12. J. Liu, M. De Bastiani, E. Aydin, G. T. Harrison, Y. Gao, R. R. Pradhan, et al, *Science*, 2022, **377**, 302-306.

13. S. Gharibzadeh, B. Abdollahi Nejand, M. Jakoby, T. Abzieher, D. Hauschild, S. Moghadamzadeh, et al, *Adv. Energy Mater.*, 2019, **9**, 1803699.

14. Y. An, N. Zhang, Z. Zeng, Y. Cai, W. Jiang, F. Qi, L. Ke, F. R. Lin, S.-W. Tsang, T. Shi, A. K-Y Jen and H.-L. Yip, *Adv. Mater.*, 2023, 2306568.

15. M. A. Mahmud, J. Zheng, S. Tang, G. Wang, J. Bing, A. D. Bui, et al, *Adv. Energy Mater.*, 2022, **12**, 2201672.

16. Z. Liu, J. Siekmann, B. Klingebiel, U. Rau and T. Kirchartz, *Adv. Energy Mater.*, 2021, **11** (16), 2003386.

17. F. Yang, P. Tockhorn, A. Musiienko, F. Lang, D. Menzel, R. Macqueen, et al., *Adv. Mater.*, 2023, 2307743.

18. C. -Y. Chen, J. -H. Chang, K. -M. Chiang, H. -L. Lin, S. -Y. Hsiao and H. -W. Lin, *Adv. Funct. Mater.*, 2015, **25**, 7064-7070.

19. J. Dagar, S. Castro-Hermosa, G. Lucarelli, F. Cacialli and T. M. Brown, *Nano Energy*, 2018, **49**, 290-299 .

20. M. Li, C. Zhao, Z.-K. Wang, C.-C. Zhang, H. K. H. Lee, A. Pockett, J. Barbé, W. C. Tsoi, Y.-G. Yang, M. J. Carnie, X.-Y. Gao, W.-X. Yang, J. R. Durrant, L.-S. Liao and S. M. Jain, *Adv. Energy Mater.*, 2018, **8**, 1801509 .

21. R. Cheng, C. -C. Chung, H. Zhang, F. Liu, W. -T. Wang, Z. Zhou, S. Wang, A. B. Djurišić and S. -P. Feng, *Adv. Energy Mater.*, 2019, **9**, 1901980.

22. X. He, J. Chen, X. Ren, L. Zhang, Y. Liu, J. Feng, J. Fang, K. Zhao and S. (Frank) Liu, *Adv. Mater.*, 2022, **33**, 2100770.

23. C. Teixeira, P. Spinelli, L. A. Castriotta, D. Müller, S. Öz, L. Andrade, A. Mendes, A. D. Carlo, U. Würfel, K. Wojciechowski and D. Forgács, *Adv. Funct. Mater.*, 2022, **32**, 2206761.

24. O. Y. Gong, G. S. Han, S. Lee, M. K. Seo, C. Sohn, G. W. Yoon, J. Jang, J. M. Lee, J. H. Choi, D. -K. Lee, S. B. Kang, M. Choi, N. -G. Park, D. H. Kim and H. S. Jung, *ACS Energy Lett.*, 2022, **7**, 2893-2903.

25. C. Zhang, C. Liu, Y. Gao, S. Zhu, F. Chen, B. Huang, Y. Xie, Y. Liu, M. Ma, Z. Wang, S. Wu, R. E. I. Schropp and Y. Mai, *Adv. Sci.*, 2022, **9**, 2204138.

26. C. -H. Chen, Z. -H. Su, Y. -H. Lou, Y. -J. Yu, K. -L. Wang, G. -L. Liu, Y. -R. Shi, J. Chen, J. -J. Cao, L. Zhang, X. -Y. Gao and Z. -K. Wang, *Adv. Mater.*, 2022, **34**, 200320.